


Cite this: *RSC Adv.*, 2024, 14, 7229

# Improvement of the rate capability of all-solid-state cells with Fe-based polysulfide positive electrode materials by modifying the microstructure†

Tomonari Takeuchi, <sup>\*a</sup> Noboru Taguchi, <sup>a</sup> Mitsunori Kitta, <sup>a</sup> Toyonari Yaji,<sup>b</sup> Misae Otoyama, <sup>a</sup> Kentaro Kuratani <sup>a</sup> and Hikari Sakaeb <sup>ac</sup>

Received 18th December 2023  
Accepted 15th February 2024

DOI: 10.1039/d3ra08641k

rsc.li/rsc-advances

We successfully prepared an Fe- and Li-containing polysulfide positive electrode material ( $\text{Li}_8\text{FeS}_5\text{--Li}_2\text{FeS}_2$  composite) that shows a high specific capacity ( $>500 \text{ mA h g}^{-1}$ ) with improved rate capability in all-solid-state cells. High-resolution TEM analysis indicated the coexistence of small crystallites of high-conductivity  $\text{Li}_2\text{FeS}_2$  and FeS, as well as low-crystallinity  $\text{Li}_2\text{S}$ , in the composite, and this microstructure is responsible for the improved battery performance.

## Introduction

Recently, there has been an increasing demand for high-energy storage systems, particularly those applicable in electric vehicles. Currently, next-generation batteries are required with a much higher energy density than that of the conventional lithium-ion batteries consisting of oxide-based cathode materials (practically *ca.*  $200 \text{ W h kg}^{-1}$ ).<sup>1,2</sup> To date, several candidates such as lithium–oxygen batteries (theoretically *ca.*  $3500 \text{ W h kg}^{-1}$ ),<sup>3,4</sup> lithium–sulphur (Li–S) batteries (*ca.*  $2600 \text{ W h kg}^{-1}$ ),<sup>5</sup> and Zn–oxygen batteries (*ca.*  $1100 \text{ W h kg}^{-1}$ )<sup>6</sup> have been included in next-generation batteries. Among them, the Li–S battery is a promising system that generates high energy density in a closed system (without introducing gaseous components).

Lithium sulphide ( $\text{Li}_2\text{S}$ ) is a potential cathode active material in Li–S cells with a high theoretical capacity (*ca.*  $1170 \text{ mA h g}^{-1}$ ) and has the advantage that a variety of anode materials such as graphite and silicon can be used in practical battery systems.<sup>7–13</sup> However,  $\text{Li}_2\text{S}$  shows high electrical resistivity, which gives rise to poor material usage in the cells. In order to enhance the conductivity of  $\text{Li}_2\text{S}$ , several attempts such as forming composites with carbon ( $\text{Li}_2\text{S–C}$ )<sup>10–12</sup> or metals ( $\text{Li}_2\text{S–Fe}$ ,  $\text{Li}_2\text{S–Cu}$ , and  $\text{Li}_2\text{S–V}$ )<sup>7–9</sup> have been made. Along with the latter material design, we developed the Fe-containing polysulfide

material  $\text{Li}_x\text{FeS}_y$ , which showed a relatively high specific capacity of *ca.*  $730 \text{ mA h g}^{-1}$  for the  $\text{Li}_8\text{FeS}_5$  cell with a non-aqueous liquid electrolyte.<sup>9</sup> However, these  $\text{Li}_x\text{FeS}_y$  cells showed capacity degradation with cycling, as observed often for Li–S cells with a liquid electrolyte, partly because of the side reactions between the sulphide electrode material and the liquid electrolyte and partly because of the dissolution of polysulfides formed during electrochemical charge/discharge reactions into the liquid electrolyte. Replacing the liquid electrolyte with the solid electrolyte is a promising approach to solve these problems, and there have been many reports on all-solid-state cells with metal polysulfide cathode materials such as  $\text{Li}_2\text{TiS}_3$ ,  $\text{Li}_3\text{NbS}_4$ , and  $\text{Li}_3\text{CuS}_2$ , showing superior electrochemical performances.<sup>14–16</sup> Much recently, V-containing polysulfide materials ( $\text{Li}_x\text{VS}_y$ ) have been developed, and their all-solid-state cells showed superior rate capability with a higher specific capacity ( $>600 \text{ mA h g}^{-1}$ ), which originated from its higher electrical conductivity ( $>10^{-2} \text{ S cm}^{-1}$ ).<sup>17</sup>

In this study, we prepared an Fe-based polysulfide electrode material ( $\text{Li}_x\text{FeS}_y$ ) in an attempt to show superior rate capability with high specific capacity in all-solid-state cells. Fe-based electrode materials are advantageous from the standpoints of resource abundance and cost, which would be beneficial for application to batteries, particularly in electric vehicles. However,  $\text{Li}_x\text{FeS}_y$  showed a relatively low conductivity of *ca.*  $1.0 \times 10^{-5} \text{ S cm}^{-1}$  for  $\text{Li}_8\text{FeS}_5$ , implying a necessity for improvement in performance, particularly in rate capability. The lower conductivity of  $\text{Li}_8\text{FeS}_5$  so far (denoted as  $\text{Li}_8\text{FeS}_5\text{–H}$  sample) is partly due to the rather homogeneous component originating from the preparation process of both heating and milling. We prepared “inhomogeneous”  $\text{Li}_8\text{FeS}_5$ , that is, coexisting with some high-conductivity components such as FeS and  $\text{Li}_2\text{FeS}_2$  by “incomplete” milling of  $\text{Li}_2\text{S}$  and FeS (denoted as  $\text{Li}_8\text{FeS}_5\text{–MM}$

<sup>a</sup>National Institute of Advanced Industrial Science and Technology (AIST), Midorigaoka 1-8-31, Ikeda, Osaka 563-8577, Japan. E-mail: takeuchi.tomonari@aist.go.jp

<sup>b</sup>Synchrotron Radiation Center, Ritsumeikan University, Kusatsu, Shiga 525-8577, Japan

<sup>c</sup>Kyushu University, 6-1 Kasuga koen, Kasuga-shi, Fukuoka 816-8580, Japan

† Electronic supplementary information (ESI) available: XAFS spectra. See DOI: <https://doi.org/10.1039/d3ra08641k>



sample) to improve its conductivity; particularly,  $\text{Li}_2\text{FeS}_2$  has been reported to show a relatively high electronic conductivity and a high  $\text{Li}^+$ -diffusion coefficient,<sup>18</sup> the coexistence of which would be advantageous for improving the rate capability of  $\text{Li}_8\text{FeS}_5$ .

## Experimental

The  $\text{Li}_8\text{FeS}_5$ -MM sample was prepared by mechanical milling technique; a blended powder of  $\text{Li}_2\text{S}$  and  $\text{FeS}$  in a 4 : 1 molar ratio was mechanically milled (MM) for 5–40 h using a planetary ball mill apparatus (Fritsch Pulverisette 7) under a rotating speed of 400 rpm to yield  $\text{Li}_8\text{FeS}_5$ -MM (5–40 h) samples. The previously reported  $\text{Li}_8\text{FeS}_5$ -H with a rather homogeneous component was also prepared by heating (600 °C) and subsequent milling for 40 h, for comparison.<sup>13</sup> Since  $\text{Li}_2\text{S}$  and the resulting  $\text{Li}_8\text{FeS}_5$  are very sensitive to atmospheric moisture, all the procedures except for the heating and mechanical milling were carried out in an argon-filled glove box; the heating and mechanical milling were carried out under atmospheric conditions using an argon-filled container and a pot wherein  $\text{Li}_2\text{S}$  and  $\text{Li}_8\text{FeS}_5$  were enclosed. We also prepared the  $\text{Li}_8\text{FeS}_5$ - $\text{Li}_2\text{FeS}_2$  composite by mechanically milling the blended powder of the above-mentioned  $\text{Li}_8\text{FeS}_5$ -MM (40 h) and  $\text{Li}_2\text{FeS}_2$  in a 6 : 4 weight ratio for 1 h ( $\text{Li}_2\text{FeS}_2$  was prepared by heating  $\text{Li}_2\text{S}$  and  $\text{FeS}$  in a 1 : 1 molar ratio at 1000 °C).

The phase purity of the sample was checked using X-ray diffraction (XRD) measurements (RINT TTR-III, Rigaku, Japan) using a monochromatic  $\text{Cu K}\alpha$  radiation within the  $2\theta$  range of 10–80°. Before the measurements, each sample was covered with a Kapton film in an argon-filled glove box, and the measurements were carried out within 1 h to minimize the reaction with atmospheric moisture. Structural refinement by X-ray Rietveld analysis was carried out using the RIETAN-2000 program.<sup>19</sup> The microstructure of the sample was examined using a high-resolution TEM (Talos F200X, ThermoFisher Scientific) operating at 300 kV in scanning mode with a probe current of 300 pA. The valence state and local structure of S atoms for the sample powders were examined by S K-edge X-ray absorption fine structure (XAFS) measurements, which were carried out at the soft X-ray double crystal monochromator beamline, BL-10, of the Synchrotron Radiation Center, Ritsumeikan University.<sup>20</sup> The total electron yield (TEY) method was used, and the incident X-ray beam was monochromatized with a Ge (111) crystal ( $2d = 6.532 \text{ \AA}$ ) pair. The photon energy was calibrated with the strong resonance of  $\text{K}_2\text{SO}_4$  ( $\text{S } 1s \rightarrow t_2$ ) appearing at 2481.7 eV.<sup>21</sup> All samples were sealed in an argon-filled transfer vessel.<sup>20</sup>

The electrical conductivity of each sample was measured using an electrochemical test device (Celltest 1470E, Solartron Analytical) with applied voltages of 50, 100, and 150 mV, after the sample powder was cold-pressed into a pellet with a diameter of 10 mm and thickness of 0.7 mm. The all-solid-state cells (10 mm in diameter) were assembled using the above-mentioned  $\text{Li}_8\text{FeS}_5$ -MM or  $\text{Li}_8\text{FeS}_5$ - $\text{Li}_2\text{FeS}_2$  by uniaxial pressing in the same manner as described previously.<sup>17</sup> Argyrodite-type sulfide solid electrolyte (SE) powder (80 mg) was

pelletized and the positive electrode powder (5 mg), which was prepared by blending  $\text{Li}_8\text{FeS}_5$ -MM (or  $\text{Li}_8\text{FeS}_5$ - $\text{Li}_2\text{FeS}_2$ ), SE, and acetylene black (AB) in a 4 : 5 : 1 weight ratio, was loaded on the above-mentioned SE pellet, which were then pressed together under 360 MPa for 5 min into a laminated pellet. After an indium foil (9 mm diameter and 0.3 mm thick) and a lithium foil (8 mm diameter and 0.2 mm thick) were attached on the opposite side as a negative electrode, it was pressed under 90 MPa for 2 min. The unit cell element was then fastened using stainless steel rods and sealed into a solid-state cell. The electrochemical measurements were carried out at 25 °C initially with charging, after standing for 1 h on open circuit, using a TOSCAT-3100 instrument (Toyo System, Japan) at a current density of  $0.13 \text{ mA cm}^{-2}$  ( $50 \text{ mA g}^{-1}$ , corresponding to *ca.* 0.1 C) when charging, and those of 0.13, 0.25, 0.64, and  $1.3 \text{ mA cm}^{-2}$  when discharging, between 3.0 and 1.0 V. Cyclic voltammetry (CV) of the cell was also conducted in the voltage range of 1.0–3.0 V (*vs.*  $\text{Li-In}$ ) using a potentiostat/galvanostat (Model 1400, Solartron Analytical) at scan rates of 0.1 and  $0.5 \text{ mV s}^{-1}$ .

## Results and discussion

The obtained  $\text{Li}_8\text{FeS}_5$ -MM powders were greyish-black in appearance, and their XRD patterns are shown in Fig. 1(a). With increasing milling time, the initial crystalline  $\text{Li}_2\text{S}$  and  $\text{FeS}$  changed to low-crystallinity  $\text{Li}_2\text{S}$  and  $\text{FeS}$ , and finally, XRD peaks originating from  $\text{FeS}$  were not detected; the XRD pattern of  $\text{Li}_8\text{FeS}_5$ -MM (40 h) was very similar to that of the previous  $\text{Li}_8\text{FeS}_5$ -H sample. The  $\text{FeS}$  content, estimated by X-ray Rietveld analysis and listed in Table 1, decreased with milling time, accompanied by a slight decrease in the lattice parameter of  $\text{Li}_2\text{S}$ . This indicates the decomposition of  $\text{FeS}$  and the partial substitution of smaller  $\text{Fe}^{2+}$  ions ( $0.66 \text{ \AA}$ ) for  $\text{Li}^+$  ions ( $0.74 \text{ \AA}$ )<sup>22</sup> in  $\text{Li}_2\text{S}$  *via* the milling process. Therefore, the milling process decreases the crystallite size of initial  $\text{Li}_2\text{S}$  and  $\text{FeS}$ , promoting the mutual chemical reaction (in particular, the incorporation of  $\text{Fe}^{2+}$  ions in  $\text{Li}_2\text{S}$ ) and resulting in finally forming low-crystallinity rather homogeneous Fe-substituted  $\text{Li}_2\text{S}$ . The measured electrical conductivity of the  $\text{Li}_8\text{FeS}_5$ -MM samples was in the range of *ca.*  $5 \times 10^{-5}$ – $8 \times 10^{-5} \text{ S cm}^{-1}$ , as listed in Table 1, which was higher than that of the  $\text{Li}_8\text{FeS}_5$ -H sample (*ca.*  $1.0 \times 10^{-5} \text{ S cm}^{-1}$ ), probably due to the coexistence of small amounts of  $\text{FeS}$  (*ca.*  $10^1 \text{ S cm}^{-1}$ )<sup>23</sup> and the incorporation of  $\text{Fe}^{2+}$  ions into  $\text{Li}_2\text{S}$ .

Fig. 1(b) shows the charge and discharge curves of the  $\text{InLi}/\text{Li}_8\text{FeS}_5$ -MM sample cells at different current densities. Data for the  $\text{InLi}/\text{Li}_8\text{FeS}_5$ -H sample cell are also shown for comparison. All the sample cells showed discharge plateaus at *ca.* 1.5 V, which corresponded to that at *ca.* 2.1 V in the previously reported  $\text{Li}/\text{Li}_8\text{FeS}_5$ -H sample cells with a non-aqueous liquid electrolyte.<sup>13</sup> The  $\text{Li}_8\text{FeS}_5$ -MM sample cells showed a higher discharge capacity, particularly at a higher current density, than that of the  $\text{Li}_8\text{FeS}_5$ -H sample cell. The specific discharge capacity at a lower current density ( $0.13 \text{ mA cm}^{-2}$ ) for the  $\text{Li}_8\text{FeS}_5$ -MM (20 h) sample cell (*ca.*  $660 \text{ mA h g}^{-1}$ ) was comparable to that of the previously reported  $\text{Li}_8\text{FeS}_5$ -H sample cell (*ca.*  $730 \text{ mA h g}^{-1}$ ) with a non-aqueous liquid electrolyte.<sup>13</sup> In



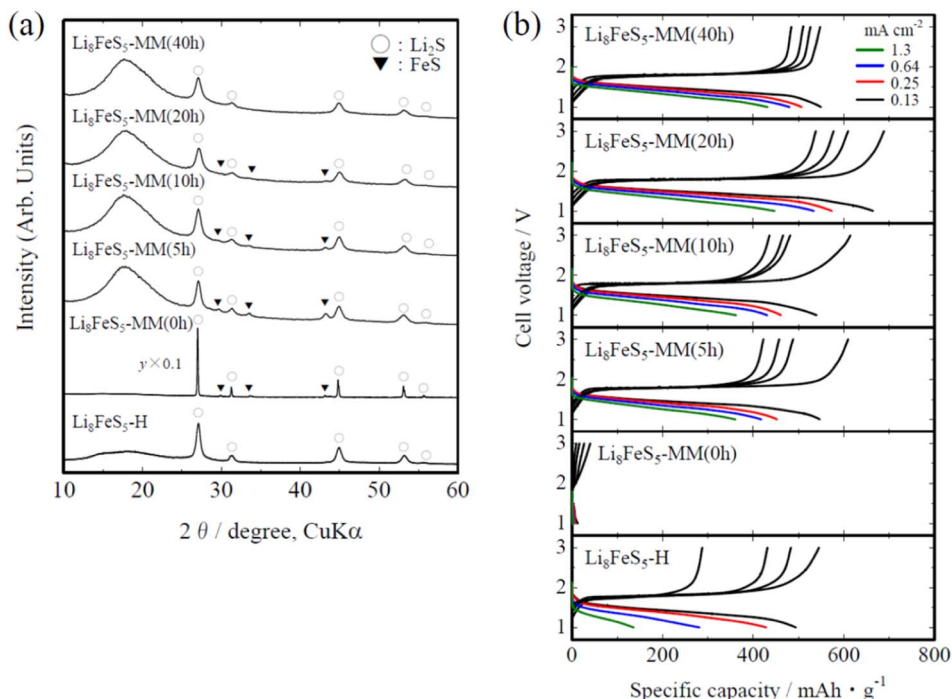


Fig. 1 (a) XRD patterns ( $\text{Cu K}\alpha$  radiation) and (b) charge and discharge profiles for the  $\text{Li}_8\text{FeS}_5\text{-MM}$  (0–40 h) sample cells at different current densities in the range of 0.13–1.3  $\text{mA cm}^{-2}$  (50–500  $\text{mA g}^{-1}$ , corresponding to ca. 0.1–1 C). Data for the  $\text{Li}_8\text{FeS}_5\text{-H}$  sample cell are also shown for comparison.

**Table 1** FeS content (mol%) and lattice parameter ( $a/\text{\AA}$ ) of  $\text{Li}_2\text{S}$  estimated by X-ray Rietveld analyses for the  $\text{Li}_8\text{FeS}_5\text{-MM}$  and  $\text{Li}_8\text{FeS}_5\text{-Li}_2\text{FeS}_2$  composite samples. The measured electrical conductivity values ( $\sigma/\text{S cm}^{-1}$ ) are also listed. Data for the previous  $\text{Li}_8\text{FeS}_5\text{-H}$  sample are also listed for comparison<sup>13</sup>

	FeS content/mol%	$a/\text{\AA}$	$\sigma/\text{S cm}^{-1}$
$\text{Li}_8\text{FeS}_5\text{-MM}$ (0 h)	4(1)	5.71112 (9)	$<10^{-8}$
$\text{Li}_8\text{FeS}_5\text{-MM}$ (5 h)	8(1)	5.710 (7)	$5.0 \times 10^{-5}$
$\text{Li}_8\text{FeS}_5\text{-MM}$ (10 h)	4(1)	5.709 (7)	$5.8 \times 10^{-5}$
$\text{Li}_8\text{FeS}_5\text{-MM}$ (20 h)	3(1)	5.704 (8)	$8.4 \times 10^{-5}$
$\text{Li}_8\text{FeS}_5\text{-MM}$ (40 h)	0(1)	5.704 (6)	$7.4 \times 10^{-5}$
$\text{Li}_8\text{FeS}_5\text{-Li}_2\text{FeS}_2$	6(1)	5.711 (3)	$4.4 \times 10^{-4}$
$\text{Li}_8\text{FeS}_5\text{-H}^{13}$	0(1)	5.7048 (10)	$1.0 \times 10^{-5}$

addition, the discharge capacity at higher current densities (ca. 450  $\text{mAh g}^{-1}$  at 1.3  $\text{mA cm}^{-2}$  for  $\text{Li}_8\text{FeS}_5\text{-MM}$  (20 h)) was comparable or superior to the previously reported values for all-solid-state Li-S batteries.<sup>14–17</sup>

Thus, the coexistence of the conductive component (FeS) in  $\text{Li}_8\text{FeS}_5$  was effective for improving the rate capability of the all-solid-state cell. We then intended to introduce another conductive component,  $\text{Li}_2\text{FeS}_2$ , to obtain the  $\text{Li}_8\text{FeS}_5\text{-Li}_2\text{FeS}_2$  composite;  $\text{Li}_2\text{FeS}_2$  additives would be advantageous for improving both the electronic conductivity and  $\text{Li}^+$  diffusion in the composite.<sup>17</sup> Fig. 2(a) shows the XRD pattern of the obtained  $\text{Li}_8\text{FeS}_5\text{-Li}_2\text{FeS}_2$  composite. As in the above-mentioned  $\text{Li}_8\text{FeS}_5\text{-MM}$  samples, the  $\text{Li}_8\text{FeS}_5\text{-Li}_2\text{FeS}_2$  composite consisted of low-crystallinity  $\text{Li}_2\text{S}$  and small amounts of FeS. No XRD peaks originating from  $\text{Li}_2\text{FeS}_2$  were detected, probably due to its

decomposition and conversion to FeS as well as its incorporation into  $\text{Li}_2\text{S}$  (resulting in Fe-substituted  $\text{Li}_2\text{S}$ ) via the milling process. The FeS content and the lattice parameter of  $\text{Li}_2\text{S}$ , estimated by the X-ray Rietveld analysis, are also listed in Table 1; judging from the data, the  $\text{Li}_8\text{FeS}_5\text{-Li}_2\text{FeS}_2$  composite seems very similar to the  $\text{Li}_8\text{FeS}_5\text{-MM}$  (5–10 h) samples. Fig. 2(b) shows the charge and discharge curves of the  $\text{Li}_8\text{FeS}_5\text{-Li}_2\text{FeS}_2$  sample cells at different current densities. Even at a higher current density, the cell showed high discharge capacity compared with the  $\text{Li}_8\text{FeS}_5\text{-MM}$  sample cells (Fig. 1(b)). Such improved rate capability is evident from the capacity retention, as shown in Fig. 2(c). CV measurements also showed consistent results; as shown in Fig. 2(d), the  $\text{Li}_8\text{FeS}_5\text{-H}$  sample cell showed a reductive peak at ca. 1.4 V under 0.1  $\text{mV s}^{-1}$  but not obvious at a higher scan rate (0.5  $\text{mV s}^{-1}$ ), whereas the  $\text{Li}_8\text{FeS}_5\text{-Li}_2\text{FeS}_2$  sample cell showed an evident peak even under a higher scan rate. The measured electrical conductivity of the  $\text{Li}_8\text{FeS}_5\text{-Li}_2\text{FeS}_2$  composite was ca.  $4.4 \times 10^{-4} \text{ S cm}^{-1}$ , higher than that of the  $\text{Li}_8\text{FeS}_5\text{-MM}$  samples (ca.  $5\text{--}8 \times 10^{-5} \text{ S cm}^{-1}$ ). Such higher conductivity is responsible for the improved rate capability in the  $\text{Li}_8\text{FeS}_5\text{-Li}_2\text{FeS}_2$  sample cell. In addition, the  $\text{Li}_8\text{FeS}_5\text{-Li}_2\text{FeS}_2$  sample cell showed improved cycle performance, as shown in Fig. 2(e) and (f), partly due to its higher conductivity; higher conductivity could improve the utilization of the active materials as well as suppress the localized charging inhomogeneity. Because the XRD results showed similar estimated FeS contents and lattice parameters of  $\text{Li}_2\text{S}$  for the  $\text{Li}_8\text{FeS}_5\text{-Li}_2\text{FeS}_2$  and  $\text{Li}_8\text{FeS}_5\text{-MM}$  (5–10 h) samples (Table 1), there would be some characteristic microstructures that cause the difference in



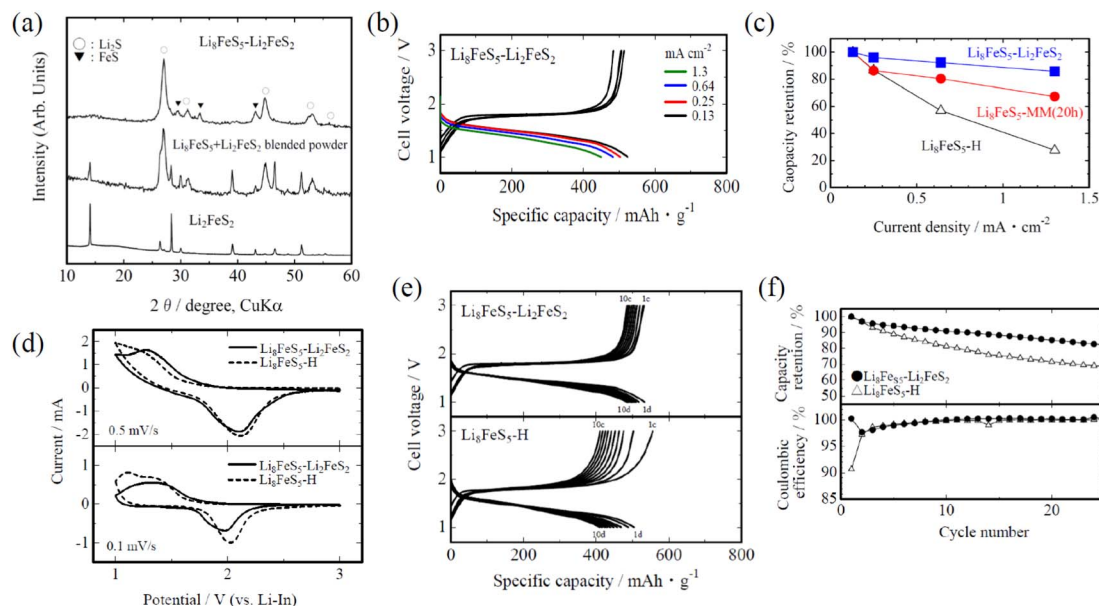


**Fig. 2** (a) XRD patterns (Cu  $K\alpha$  radiation) of the  $\text{Li}_2\text{FeS}_2$ ,  $\text{Li}_8\text{FeS}_5 + \text{Li}_2\text{FeS}_2$  blended powder, and  $\text{Li}_8\text{FeS}_5\text{-Li}_2\text{FeS}_2$  composite samples. (b) Charge and discharge profiles of the  $\text{Li}_8\text{FeS}_5\text{-Li}_2\text{FeS}_2$  sample cell at different current densities in the range of  $0.13\text{--}1.3\text{ mA cm}^{-2}$  ( $50\text{--}500\text{ mA g}^{-1}$ , corresponding to ca.  $0.1\text{--}1\text{ C}$ ). (c) Capacity retention at different current densities for the  $\text{Li}_8\text{FeS}_5\text{-H}$ ,  $\text{Li}_8\text{FeS}_5\text{-MM}$  (20 h), and  $\text{Li}_8\text{FeS}_5\text{-Li}_2\text{FeS}_2$  sample cells. (d) CV profiles at  $0.1$  and  $0.5\text{ mV s}^{-1}$ , (e) charge and discharge profiles (10 cycles), and (f) capacity retention and coulombic efficiency of the  $\text{Li}_8\text{FeS}_5\text{-Li}_2\text{FeS}_2$  and  $\text{Li}_8\text{FeS}_5\text{-H}$  sample cells at a current density of  $0.13\text{ mA cm}^{-2}$ .

the XAFS measurements and TEM observations for the  $\text{Li}_8\text{FeS}_5\text{-Li}_2\text{FeS}_2$  sample.

Fig. S1† shows the S K-edge X-ray absorption near-edge structure (XANES) spectra of the  $\text{Li}_8\text{FeS}_5\text{-Li}_2\text{FeS}_2$  and  $\text{Li}_8\text{FeS}_5\text{-H}$  samples. Both samples showed similar spectra with three characteristic absorption peaks at  $2469\text{ eV}$  (assigned to the bound state resonance due to an electronic transition between the S  $1s$  and p-hybridized Fe  $3d$  bands),  $2472\text{--}2473\text{ eV}$  (originating from the  $1s \rightarrow 3p$  electronic transition in sulphur

atoms), and  $2476\text{ eV}$  (originating from the electronic transition of the  $1s$  electron in  $\text{S}^{2-}$  to the unoccupied orbital with S  $3p$  and Li  $2s$  characters).<sup>13,24</sup> These spectral similarities indicate that the valence state and local structure around the S atoms are nearly consistent among these samples; that is, the Fe, Li, and S atoms surrounding the S atoms coordinate in a similar configuration on average while including slight fluctuations individually.

In contrast to the XAFS results, TEM observations showed a characteristic microstructure in the  $\text{Li}_8\text{FeS}_5\text{-Li}_2\text{FeS}_2$  sample. As

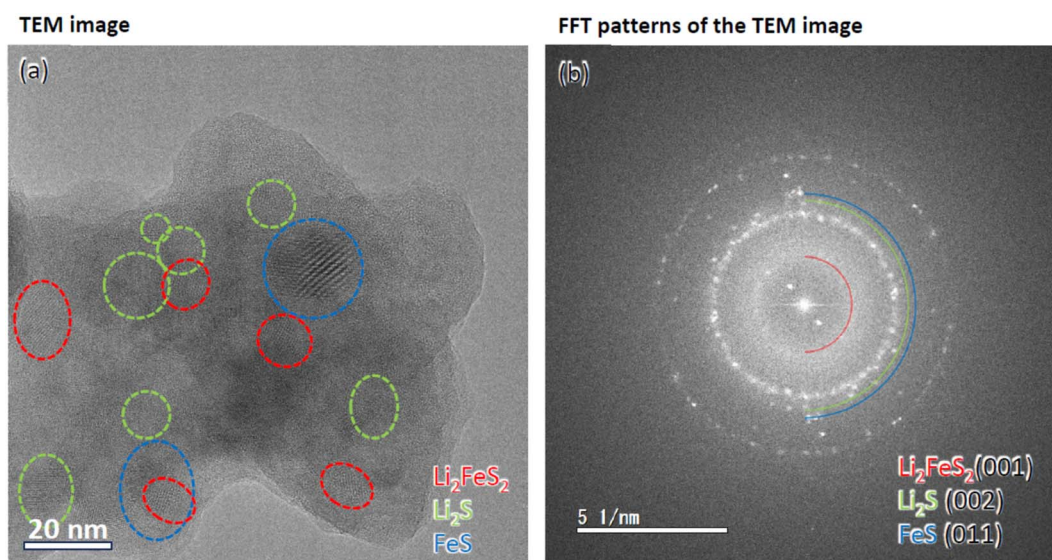


**Fig. 3** (a) High-resolution TEM image and (b) fast Fourier transform (FFT) patterns of the TEM image for the  $\text{Li}_8\text{FeS}_5\text{-Li}_2\text{FeS}_2$  sample. Several semicircles corresponding to the Debye-Scherrer rings originating from  $\text{Li}_2\text{FeS}_2(001)$ ,  $\text{Li}_2\text{S}(002)$ , and  $\text{FeS}(011)$  are shown as examples.



shown in Fig. 3(a), the high-resolution TEM images showed the presence of some lattice fringes with domain sizes of *ca.* 10–20 nm distributed randomly in the amorphous (non-crystalline) background in the  $\text{Li}_8\text{FeS}_5\text{--Li}_2\text{FeS}_2$  sample. In order to confirm the structure of each lattice fringe, the fast Fourier transform (FFT) pattern (pseudo diffraction pattern) of the TEM image was obtained (Fig. 3(b)), where several Debye–Scherrer rings and a halo pattern were observed. By careful comparison of the lattice spacings with previously reported crystallographic data,<sup>25</sup> they were assigned to the  $\text{Li}_2\text{S}$  and  $\text{FeS}$  components (for example, *ca.* 0.29 nm for  $\text{Li}_2\text{S}(002)$  and *ca.* 0.27 nm for  $\text{FeS}(011)$ ). A notable point is that the extra component, not assigned to  $\text{Li}_2\text{S}$  and  $\text{FeS}$ , remained, and it was assigned to  $\text{Li}_2\text{FeS}_2$  (for example, *ca.* 0.63 nm for  $\text{Li}_2\text{FeS}_2(001)$ ). Although no peaks ascribed to  $\text{Li}_2\text{FeS}_2$  were detected in the XRD pattern (Fig. 2(a)), there remained very small (or close to amorphous)  $\text{Li}_2\text{FeS}_2$  crystallites in the  $\text{Li}_8\text{FeS}_5\text{--Li}_2\text{FeS}_2$  sample. By inverse Fourier transformation of the FFT pattern, the locations of these three components ( $\text{Li}_2\text{S}$ ,  $\text{FeS}$ , and  $\text{Li}_2\text{FeS}_2$ ) were approximately identified in the TEM image and denoted in Fig. 3(a). Such a microstructure would be responsible for the higher conductivity and improved rate capability of the all-solid-state cell. Particularly, the difference in rate capability between the  $\text{Li}_8\text{FeS}_5\text{--MM}$  and  $\text{Li}_8\text{FeS}_5\text{--Li}_2\text{FeS}_2$  sample cells (Fig. 2(c)) would originate from the coexistence of small crystallites of  $\text{Li}_2\text{FeS}_2$  having higher  $\text{Li}^+$  diffusion. In addition, the difference between the  $\text{Li}_8\text{FeS}_5\text{--MM}$  (40 h) and  $\text{Li}_8\text{FeS}_5\text{--H}$  sample cells (Fig. 1(b)) (both samples showed no  $\text{FeS}$  content estimated in XRD) might be due to the coexistence of small crystallites of  $\text{FeS}$  in the  $\text{Li}_8\text{FeS}_5\text{--MM}$  (40 h) sample; the higher conductivity of the  $\text{Li}_8\text{FeS}_5\text{--MM}$  (40 h) sample indicates the coexistence of small crystallites of  $\text{FeS}$  (XRD is usually detectable for a crystallite of size more than 10 nm). Thus, designing a microstructure, in which small crystallites of high conductive and high  $\text{Li}^+$  diffusion components coexist, is effective for assembling all-solid-state cells with improved rate capability.

## Conclusions

A Fe- and Li-containing polysulfide positive electrode material ( $\text{Li}_8\text{FeS}_5\text{--Li}_2\text{FeS}_2$  composite) was successfully prepared, and it showed a high specific capacity ( $>500 \text{ mA h g}^{-1}$ ) with improved rate capability in all-solid-state cells. XRD results showed that this composite consisted of low-crystallinity  $\text{Li}_2\text{S}$  and  $\text{FeS}$ , whereas high-resolution TEM analysis indicated the coexistence of small crystallites of  $\text{Li}_2\text{S}$ ,  $\text{FeS}$ , and  $\text{Li}_2\text{FeS}_2$ . This microstructure, in which highly conductive and high  $\text{Li}^+$  diffusion components coexist, resulted in higher electrical conductivity and improved rate capability in all-solid-state cells.

## Conflicts of interest

There are no conflicts to declare.

## Acknowledgements

This work is based on the results obtained from a project, SOLID-EV (JPNP18003), subsidized by the New Energy and Industrial Technology Development Organization (NEDO).

## References

- 1 X. Ji and L. F. Nazar, *J. Mater. Chem.*, 2010, **20**, 9821–9826.
- 2 P. G. Bruce, S. A. Freunberger, L. J. Hardwick and J.-M. Tarascon, *Nat. Mater.*, 2012, **11**, 19–29.
- 3 Y.-X. Yu, *J. Phys. Chem. C*, 2019, **123**, 205–213.
- 4 J.-H. Li, J. Wu and Y.-X. Yu, *J. Mater. Chem. A*, 2021, **9**, 10186.
- 5 P. Das and P. Sarkar, *Phys. Chem. Chem. Phys.*, 2023, **25**, 30536.
- 6 K. A. J. Dilshad and M. K. Rabinal, *Phys. Chem. Chem. Phys.*, 2023, **25**, 11566.
- 7 M. N. Obrovac and J. R. Dahn, *Electrochem. Solid-State Lett.*, 2002, **5**, A70–A73.
- 8 A. Hayashi, R. Ohtsubo, T. Ohtomo, F. Mizuno and M. Tatsumisago, *J. Power Sources*, 2008, **183**, 422–426.
- 9 T. Shigedomi, Y. Fujita, T. Kishi, K. Motohashi, H. Tsukasaki, H. Nakajima, S. Mori, M. Tatsumisago, A. Sakuda and A. Hayashi, *Chem. Mater.*, 2022, **34**, 9745–9752.
- 10 M. Nagao, A. Hayashi and M. Tatsumisago, *J. Mater. Chem.*, 2012, **22**, 10015–10020.
- 11 T. Takeuchi, H. Kageyama, K. Nakanishi, M. Tabuchi, H. Sakaebe, T. Ohta, H. Senoh, T. Sakai and K. Tatsumi, *J. Electrochem. Soc.*, 2010, **157**, A1196–A1201.
- 12 K. Han, J. Shen, C. M. Hayner, H. Ye, M. C. Kung and H. H. Kung, *J. Power Sources*, 2014, **251**, 331–337.
- 13 T. Takeuchi, H. Kageyama, K. Nakanishi, M. Ogawa, T. Ohta, A. Sakuda, H. Sakaebe, H. Kobayashi and Z. Ogumi, *J. Electrochem. Soc.*, 2015, **162**, A1745–A1750.
- 14 A. Sakuda, T. Takeuchi, M. Shikano, H. Sakaebe and H. Kobayashi, *Front. Energy Res.*, 2016, **4**, 1–7.
- 15 A. Sakuda, T. Takeuchi, K. Okamura, H. Kobayashi, H. Sakaebe, K. Tatsumi and Z. Ogumi, *Sci. Rep.*, 2014, **4**, 4883.
- 16 Y. Kawasaki, H. Tsukasaki, T. Ayama, S. Mori, M. Deguchi, M. Tatsumisago, A. Sakuda and A. Hayashi, *ACS Appl. Energy Mater.*, 2021, **4**, 20–24.
- 17 M. Otoyama, T. Takeuchi, N. Taguchi, K. Kuratani and H. Sakaebe, *ECS Adv.*, 2023, **2**, 010501.
- 18 C. D. Wei, H. T. Xue, X. D. Zhao and F. L. Tang, *Phys. Chem. Chem. Phys.*, 2023, **25**, 8515–8523.
- 19 F. Izumi and T. Ikeda, *Mater. Sci. Forum*, 2000, **321**, 198–203.
- 20 K. Nakanishi, S. Yagi and T. Ohta, *AIP Conf. Proc.*, 2010, **1234**, 931.
- 21 M. Kiguchi, T. Yokoyama, D. Matsumura, H. Kondoh, T. Ohta and Y. Kitajima, *Phys. Rev. B: Condens. Matter Mater. Phys.*, 1999, **60**, 16205–16210.
- 22 R. D. Shannon, *Structure and Bonding in Crystals*, Academic Press. Inc., 1981, vol. ii, pp. 53–70.
- 23 H. Kobayashi, N. Takeshita, N. Mori, H. Takahashi and T. Kamimura, *Phys. Rev. B: Condens. Matter Mater. Phys.*, 2001, **63**, 115203.
- 24 S. Bodeur and J. M. Esteva, *Chem. Phys.*, 1985, **100**, 415–427.
- 25 ICSD (Inorganic Crystal Structure Database) code 68380 ( $\text{Li}_2\text{FeS}_2$ ), 168079 ( $\text{FeS}$ ), and 409397 ( $\text{Li}_2\text{S}$ ).

